Research Square

Preprints are preliminary reports that have not undergone peer review.
They should not be considered conclusive, used to inform clinical practice,
or referenced by the media as validated information.

S-Shaped Bifurcation Cascades and Loop Proliferation in an Active Magnetic Bearing Rotor with Cubic Shaft Stiffness and Nonlinear Aerodynamic Drag

Farouk Thaljaoui

farouk.thaljawi@gmail.com

University of Carthage

Thabet Guesmi

University of Gafsa

Thaljaoui Wathek

institut supérieur des études technologiques de Sidi Bouzid

Research Article

Keywords: Nonlinear dynamics, Bifurcation diagrams, Stability analysis, AMB rotors

Posted Date: August 5th, 2026

DOI: https://doi.org/10.21203/rs.3.rs-10594457/v1

License: This work is licensed under a Creative Commons Attribution 4.0 International License.
Read Full License

Additional Declarations: The authors declare no competing interests.

S-Shaped Bifurcation Cascades and Loop Proliferation in an Active Magnetic Bearing Rotor with Cubic Shaft Stiffness and Nonlinear Aerodynamic Drag

Farouk Thaljaoui[1,2*], Thabet Guesmi[3,4†] and Wathek Thaljaoui[5,6†]

[1*]Department of Mechanical Engineering, Tunisia Polytechnic School, University of Carthage, B.P.743, La Marsa, 2078, Tunis, Tunisia.
[2]Applied Mechanics and Systems Research Laboratory, Tunisia Polytechnic School, University of Carthage, B.P.743, La Marsa, 10587, Tunis, Tunisia.
[3]Department of Physics, Faculty of Science of Gafsa, University of Gafsa, 2112, Gafsa, Tunisia.
[4]Laboratory of Technology, Energy and Innovative Materials, Faculty of Science of Gafsa, University of Gafsa, 2112, Gafsa, Tunisia.
[5]Department of Mechanical Engineering, Higher Institute of Technological Studies of Sidi Bouzid, B.P.377, 9100, Sidi Bouzid, Tunisia.
[6]Department of Forensic Sciences , Faculty of Medicine of Sousse, 4002, Sousse, Tunisia.

*Corresponding author(s). E-mail(s): farouk.thaljawi@gmail.com;
Contributing authors: gasmithabet.thabet@gmail.com;
thaljawiwathek@yahoo.fr;
†These authors contributed equally to this work.

Abstract

This paper investigates the nonlinear dynamic response of a flexible rotor supported by active magnetic bearings (AMBs), incorporating cubic shaft stiffness and nonlinear aerodynamic drag, using the Harmonic Quadrature Method (HQM) combined with pseudo-arc-length continuation and Floquet stability analysis. The governing equations, derived via Lagrange formalism and non-dimensionalized, yield a coupled four-degree-of-freedom system in which disk

and journal dynamics interact through nonlinear shaft forces and nonlinear electromagnetic forces governed by proportional-derivative (PD) feedback. Four key parameters are systematically investigated. Increasing the proportional gain P drives a progressive bifurcation cascade through four regimes, linear, 1S-, 2S-, and 3S-shaped, each transition accompanied by an increasing number of Floquet-verified saddle-node bifurcations and a widening multi-stable frequency band, with the primary resonance amplitude rising from 0.2328 to 0.3839 as P increases from 2 to 4. The derivative gain D produces an exact inverse cascade, destroying the S-shaped multi-stability and restoring quasi-linear behavior for $D \geq 1.23$, revealing complementary and nearly symmetric roles between the two gains. Increasing the nonlinear stiffness coefficient η_{NL} at fixed P introduces a hardening mechanical nonlinearity that competes with the softening magnetic nonlinearity, generating a connected closed-loop branch with more than 36 saddle-node bifurcations spanning $\Omega \in [0.2466, 0.2922]$, confirmed by force comparison showing the cubic-to-magnetic force ratio rising from 0.002% to 8.6% at loop onset. Finally, an amplitude-dependent aerodynamic damping transition is identified, nonlinear turbulent damping governs the primary resonance while linear viscous damping controls superharmonic peaks. These findings characterize the nonlinear bifurcation topology of AMB-rotor systems under combined nonlinearities, with direct implications for PD controller tuning and rotor dynamic prediction.

Keywords: Nonlinear dynamics, Bifurcation diagrams, Stability analysis, AMB Rotors

1 Introduction

Active magnetic bearings (AMBs) have become an increasingly important support technology in high-speed rotating machinery, including turbomolecular pumps, machine tool spindles, flywheel energy storage systems, and aeroengine applications. Unlike conventional rolling-element or hydrodynamic bearings, AMBs suspend the rotor through a controlled electromagnetic force, eliminating mechanical contact and the associated wear, lubrication requirements, and friction losses. This contactless suspension is achieved through active feedback control, typically of proportional–derivative (PD) form, which continuously adjusts the coil currents to maintain the rotor at its equilibrium position. However, the electromagnetic force generated by an AMB is inherently nonlinear, being inversely proportional to the square of the air gap, and this nonlinearity becomes increasingly significant as the control gains are increased or as the rotor displacement approaches the nominal air gap. The practical importance of a robust AMB control design has been demonstrated experimentally: [1] compared classical PID control against LQG/LTR compensators on a 2-DOF radial AMB test rig, confirming that the choice of control architecture directly governs achievable disturbance rejection and overshoot, while [2] reported the mechanical development and control of a high-speed AMB-supported turbogenerator shaft, validating stable operation up to industrially relevant speeds. Consequently, the robust design of AMB-supported rotors requires a thorough understanding of the nonlinear

dynamic phenomena that the electromagnetic force nonlinearity can induce, particularly when combined with other nonlinear mechanisms inherent to flexible rotor systems, such as nonlinear shaft stiffness and nonlinear aerodynamic drag.

Several studies have investigated the nonlinear dynamic behavior of AMB-supported rotor systems arising from the electromagnetic force nonlinearity. [3] considered a rigid disk-rotor supported by AMBs without gyroscopic effects and examined the primary resonance response under multiple excitation forces; applying the method of multiple scales, the study reported multi-valued solutions and a jump phenomenon near resonance, with the steady-state amplitude decreasing monotonically with the natural frequency and the linear damping coefficient. [4] examined a rotor-AMB system coupled to touchdown bearings under strong base shock excitation, modeling the contact forces through Hertzian theory together with a saturating PD controller; the results identified three distinct post-shock motion regimes, with periodic, quasi-periodic, and jump-type responses depending on the unbalance eccentricity, radial clearance, and equivalent bearing stiffness and damping. [5] investigated a flexible rotor-shaft-AMB system subject to periodic base motion and applied Floquet–Liapunov theory to assess parametric stability, showing that a conventional PID control law leaves the system only marginally stable under such excitation, whereas a proposed viscoelastic-inspired control law achieved full stabilization with lower control effort. [6] studied a magnetically supported coaxial rotor operating in auxiliary bearings and showed, through bifurcation diagrams and Lyapunov exponent analysis, that increasing the shaft or auxiliary bearing stiffness can drive the system from periodic into quasi-periodic or chaotic motion. [7] examined a four-degree-of-freedom rotor-AMB system near internal resonance and showed that a standard PD current controller alone permits large-amplitude, multi-valued, jump-prone responses, whereas an additional nonlinear saturation controller was able to suppress these phenomena almost entirely. These studies collectively establish that the PD control gains, and the electromagnetic force nonlinearity they regulate, are not merely stabilizing parameters but can themselves act as bifurcation parameters governing the onset of multi-valued, jump-prone frequency responses.

In parallel, a substantial body of literature has addressed the role of mechanical shaft nonlinearities in shaping rotor frequency response. [8] examined the torsional dynamics of an automotive driveline half-shaft incorporating cubic stiffness nonlinearity and found that a negative cubic coefficient mitigated torsional shock response while a positive coefficient worsened it, with the resonance response losing stability once the cubic coefficient exceeded a critical threshold. [9] developed a large-deflection nonlinear curvature model of a flexible rotor-disk-bearing system with geometric eccentricity and mass unbalance, demonstrating a rich sequence of periodic, quasi-periodic, period-doubling, and chaotic responses, with instability occurring through a saddle-node bifurcation producing a sudden amplitude jump. [10] studied nonlinear damping suspensions with variable damping exponents in a flexible rotor in journal bearings and found that the stabilizing effect of the damping nonlinearity depends strongly on rotor speed, with cubic damping generally outperforming linear damping at high speed. [11] investigated a flexible shaft-disk system under axial load and mass unbalance supported by nonlinear bearing stiffness, showing that the system could lose stability via

saddle-node or pitchfork bifurcation with sudden jump phenomena, and that disk-related parameters shift the instability to different frequencies. These findings confirm that cubic-type mechanical stiffness nonlinearities, whether hardening or softening, are capable of producing amplitude jumps and saddle-node bifurcations qualitatively similar to those induced by electromagnetic force nonlinearity in AMB rotors, raising the question of how the two mechanisms interact when acting simultaneously and with opposite sign.

The role of nonlinear, amplitude-dependent damping in rotating and aeroelastic systems has also received attention. [12] examined a magnetic energy-harvesting system mounted on a translating blade and showed that flutter instability could be triggered not only by increasing wind speed or decreasing mechanical damping, but also by unfavorable combinations of electrical load and electromagnetic coupling. [13] developed a nonlinear aeroelastic model of a helicopter rotor incorporating dynamic stall and an advanced wake representation and found that accounting for these nonlinear aerodynamic effects improved the correlation between predicted and experimental lag damping relative to earlier linear analyses. [14] compared time-domain and eigenvalue-based stability analyses of a coupled helicopter rotor-fuselage system and found that nonlinear time-domain simulation produced modal damping predictions in closer agreement with wind-tunnel data than linearized eigen-analysis. [15] assessed the dynamic stability of compound helicopter configurations and found that additional aerodynamic surfaces altered the damping characteristics of the natural flight modes relative to a conventional configuration. Although developed for aeroelastic and helicopter rotor systems rather than AMB-supported shafts, these studies establish that nonlinear, amplitude-dependent damping mechanisms can qualitatively change the stability and response amplitude of a rotating system, a consideration equally relevant to the aerodynamic drag acting on a high-speed AMB rotor disk.

From a methodological standpoint, frequency-domain and continuation-based methods have proven effective for capturing multi-valued periodic solutions and bifurcations in nonlinear rotordynamic systems while avoiding the computational cost of long-time direct integration. [16] combined an accelerating sweep-frequency excitation technique with transient CFD to identify rotordynamic coefficients of annular gas seals, validating the method against three published experimental configurations with a 98% reduction in computational cost at equal frequency resolution. [17] applied the harmonic balance method to the forced vibration of a geometrically nonlinear cantilever beam, validating the results against fourth-order Runge–Kutta integration and characterizing jump, bifurcation, and beat phenomena. Direct integration has also been widely employed for capturing non-periodic solutions, [18] combined a shooting/continuation algorithm with component mode synthesis, a deflation algorithm, and parallel computing to compute periodic solutions and bifurcations of a large-order rotordynamic system on nonlinear tilting-pad bearings, remaining tractable for models exceeding 150 degrees of freedom. [19] proposed a semi-analytic time-integration method for non-symmetric nonlinear rotordynamic systems, separating the solution into quasi-static and dynamic parts with modal reduction applied to the latter. More recently, the Harmonic Quadrature Method (HQM) was introduced as a periodic discretization technique that avoids costly Galerkin-type integrals while retaining

high-order accuracy [20, 21]; it was validated against literature data and applied to characterize the multi-harmonic, non-synchronous, and chaotic response of a misaligned rotor supported by ball bearings with squeeze film damping, subjected to base excitation. Building on this validated framework, HQM is combined here for the first time with pseudo-arc-length continuation and Floquet stability analysis, extending its scope from time-domain harmonic-response characterization to the direct tracking of stable and unstable periodic branches and the systematic detection of saddle-node bifurcations.

According to the preceding review, existing studies have examined the electromagnetic force nonlinearity, the cubic shaft stiffness nonlinearity, and nonlinear aerodynamic damping in AMB or flexible rotor systems largely in isolation, or in combination with only one other nonlinear mechanism at a time. The interaction of a softening electromagnetic nonlinearity with a competing hardening mechanical nonlinearity, and its combined effect with an amplitude-dependent nonlinear aerodynamic drag, has not been comprehensively characterized within a single AMB rotor model. In particular, the possibility that these competing nonlinearities may generate connected closed-loop branches with a large number of saddle-node bifurcation points distinct from the simpler S-shaped folds produced by either nonlinearity alone remains unexplored, despite its direct relevance to the safe tuning of PD control gains in practical AMB systems.

Therefore, in the present study, a flexible rotor supported by active magnetic bearings, incorporating nonlinear electromagnetic control forces, cubic shaft stiffness, and nonlinear aerodynamic drag, is considered. This paper is organized as follows: in Section 2, the nonlinear equations of motion are derived using Lagrangian formalism and cast in non-dimensional form. Section 3 presents the Harmonic Quadrature Method (HQM) combined with pseudo-arc-length continuation and Floquet stability analysis used to compute and classify the periodic solutions of the system. In Section 4, this framework is applied to investigate the effects of the proportional gain, the derivative gain, the nonlinear stiffness coefficient, and the aerodynamic damping coefficients on the system's bifurcation topology. Concluding remarks are provided in Section 5.

2 System Modeling of a Flexible Rotor Supported by Active Magnetic Bearings

2.1 System overview

The system investigated numerically is a flexible rotor supported by active magnetic bearings and rotating at the angular velocity Ω.

For numerical modeling, the rotor is idealized as a lumped mass m_D concentrated at its mid-span, with two identical journal masses m_J located at the bearing stations. The corresponding schematic representation of the rotor-bearing system is shown in Fig. 1.

The shaft stiffness is given by k_R and k_{NL} to describe respectively the one-half of the linear shaft deformation for small deflections and nonlinear shaft deformation for moderate to large deformation. The system damping is provided by aerodynamic

effects and also could be given by linear damping c_R for low air resistance and by nonlinear damping c_{NL} for high air resistance. The magnetic bearing system acts on the shaft journals through electromagnetic forces F_X and F_Y as shown in Fig. 2.

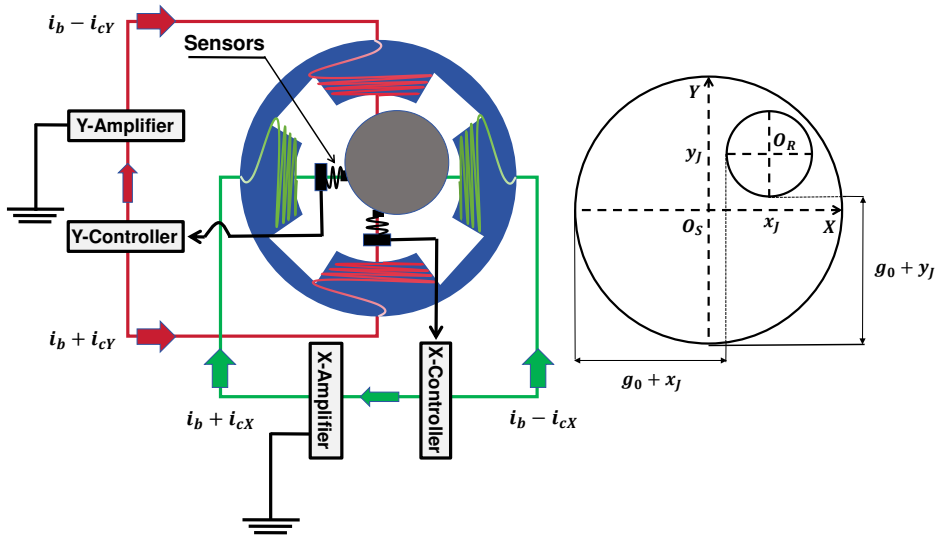

Fig. 1: Active Magnetic Bearing modeling

To derive the governing equations of motion, several simplifying assumptions are introduced. The rotor is assumed to be symmetric, with its mass distributed between the mid-span and the bearing stations, and it rotates at a constant angular velocity ω. The rotor and support stiffnesses are considered radially symmetric. Rotor imbalance is assumed to be confined to a single plane at the mid-span disk, axial motion is neglected, and gyroscopic effects are disregarded. Owing to the system symmetry, only one-half of the rotor-bearing configuration is considered in the derivation. The system dynamics are therefore described by the lateral displacements x_D and y_D of the rotor mid-span center and x_J and y_J of the journal center.

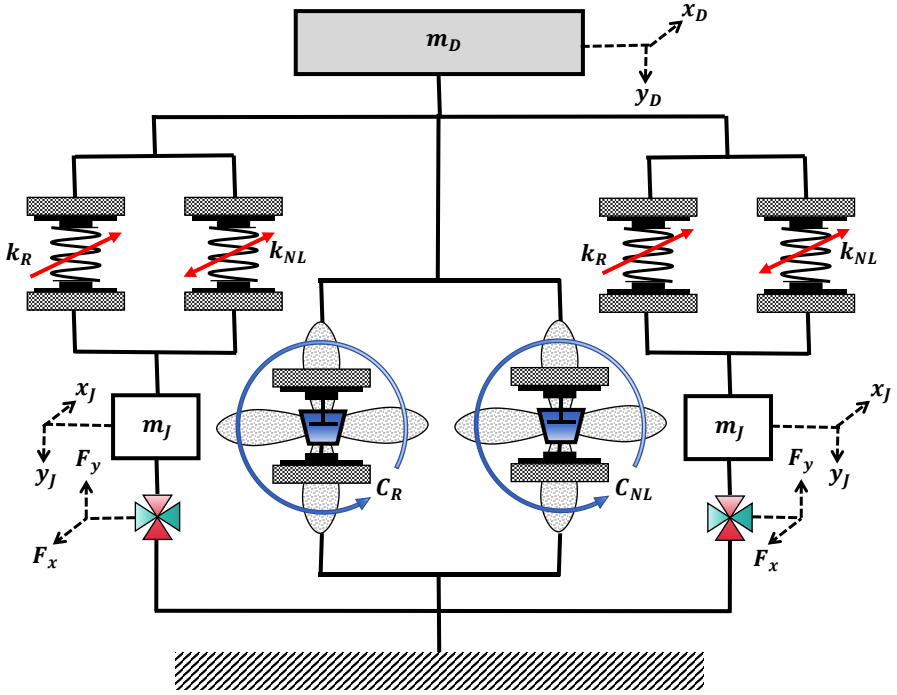

Fig. 2: Rotor shaft modeling

2.2 Energies calculation and Equations of motion elaboration

The non-conservative forces are introduced through the generalized force components F_{x_D}, F_{y_D}, F_{x_J}, and F_{y_J}, which account for the imbalance excitation acting on the disk as well as the magnetic bearing control forces applied at the journal locations. These generalized forces are expressed as:

$$\begin{aligned} F_{x_D} &= 2m_D u\Omega^2 cos(\Omega t) \\ F_{y_D} &= 2m_D u\Omega^2 sin(\Omega t) \\ F_{x_J} &= \hat{F}_X \\ F_{y_J} &= \hat{F}_Y \end{aligned} \tag{1}$$

where u denotes the eccentricity of the rotor center of mass.

Then, function of the electromagnetic coupling α, the global magnetic forces are given by :

$$\begin{aligned} \hat{F}_X &= \hat{F}_{X^+} - \hat{F}_{X^-} + \alpha\hat{x}_J \left(\hat{F}_{Y^+} + \hat{F}_{Y^-}\right) \\ \hat{F}_Y &= \hat{F}_{Y^+} - \hat{F}_{Y^-} + \alpha\hat{y}_J \left(\hat{F}_{X^+} + \hat{F}_{X^-}\right) \end{aligned} \tag{2}$$

The Electromagnetic forces are :

$$\begin{aligned}
\hat{F}_{X^+} &= \frac{\mu_0 N^2 S m_J \omega_n^2 g_0}{4} \frac{(i_{X^+})^2}{(g_0 - x_J)^2} \\
\hat{F}_{X^-} &= \frac{\mu_0 N^2 S m_J \omega_n^2 g_0}{4} \frac{(i_{X^-})^2}{(g_0 + x_J)^2} \\
\hat{F}_{Y^+} &= \frac{\mu_0 N^2 S m_J \omega_n^2 g_0}{4} \frac{(i_{Y^+})^2}{(g_0 - y_J)^2} \\
\hat{F}_{Y^-} &= \frac{\mu_0 N^2 S m_J \omega_n^2 g_0}{4} \frac{(i_{Y^-})^2}{(g_0 + y_J)^2}
\end{aligned} \tag{3}$$

Parameters N, S, μ_0, ω_n and g_0 are respectively number of coil turns, area of one magnetic pole (m), permeability of free space $(4\pi 10^{-7} H/m)$, linear natural frequency of the magnetic bearing system $\left(\sqrt{\frac{\mu_0 N^2 S i_b^2 \left(\frac{g_0}{i_b}\hat{P}-1\right)}{m_J g_0^3}}\right)$ and nominal air gap (m).

Coil currents i_{X^+}, i_{X^-}, i_{Y^+} and $i_{Y^-}$are given as :

$$\begin{aligned}
i_{X^+} &= i_b - \left(\hat{P}\hat{x}_J + \hat{D}\hat{\dot{x}}_J\right) \\
i_{X^-} &= i_b + \left(\hat{P}\hat{x}_J + \hat{D}\hat{\dot{x}}_J\right) \\
i_{Y^+} &= i_b - \left(\hat{P}\hat{y}_J + \hat{D}\hat{\dot{y}}_J\right) \\
i_{Y^-} &= i_b + \left(\hat{P}\hat{y}_J + \hat{D}\hat{\dot{y}}_J\right)
\end{aligned} \tag{4}$$

where i_b, $\hat{P}$ and $\hat{D}$ are respectively bias magnetic coil current (A), proportional feedback gain (A/m) and derivative feedback gain (As/m)

The application of Lagrange formalism for each generalized coordinate q_i, with respect to generalized force components Q_i^{ext}, is based on the following equation :

$$\frac{d}{dt}\left(\frac{\partial K}{\partial \dot{q}_i}\right) - \frac{\partial K}{\partial q_i} + \frac{\partial P}{\partial q_i} + \frac{\partial R}{\partial \dot{q}_i} = Q_i^{ext} \tag{5}$$

The Kinetic Energy is given as :

$$K = \frac{1}{2} m_D \left(\left(\hat{\dot{x}}_D\right)^2 + \left(\hat{\dot{y}}_D\right)^2\right) + \frac{1}{2} m_J \left(\left(\hat{\dot{x}}_J\right)^2 + \left(\hat{\dot{y}}_J\right)^2\right) + \frac{1}{2} I \omega^2 \tag{6}$$

For small deflections, the shaft behaves as a linear spring :

$$P_{lin} = \frac{1}{2} k_R \left[(\hat{x}_D - \hat{x}_J)^2 + (\hat{y}_D - \hat{y}_J)^2\right] \tag{7}$$

For moderate to large deflections, the shaft undergoes axial stretching. The nonlinear potential energy is:

$$P_{nl} = \frac{1}{2} k_{NL} \left[(\hat{x}_D - \hat{x}_J)^2 + (\hat{y}_D - \hat{y}_J)^2\right]^2 \tag{8}$$

The gravitational potential energy is :

$$P_{grav} = m_D g \hat{y}_D + m_J g \hat{y}_J \tag{9}$$

At low Reynolds numbers, the air flow around the disk is laminar so then the Rayleigh dissipation function is :

$$R_R = \frac{1}{2} c_R \left(\left(\hat{\dot{x}}_D \right)^2 + \left(\hat{\dot{y}}_D \right)^2 \right) \tag{10}$$

At high rotational, the air flow becomes turbulent, producing drag proportional to the square of velocity :

$$R_{NL} = \frac{1}{3} c_{NL} \sqrt{\left(\left(\hat{\dot{x}}_D \right)^2 + \left(\hat{\dot{y}}_D \right)^2 \right)^3} \tag{11}$$

The Equations of motion are then given as :

$$\begin{aligned}
m_D \hat{\ddot{x}}_D &= m_D u \omega^2 cos\left(\omega t\right) - c_R \hat{\dot{x}}_D - c_{NL} \hat{\dot{x}}_D \sqrt{\left(\hat{\dot{x}}_D \right)^2 + \left(\hat{\dot{y}}_D \right)^2} \\
&\quad - k_R \left(\hat{x}_D - \hat{x}_J \right) - k_{NL} \left(\hat{x}_D - \hat{x}_J \right) \left[\left(\hat{x}_D - \hat{x}_J \right)^2 + \left(\hat{y}_D - \hat{y}_J \right)^2 \right] \\
m_D \hat{\ddot{y}}_D &= m_D u \omega^2 sin\left(\omega t\right) - m_D g - c_R \hat{\dot{y}}_D - c_{NL} \hat{\dot{y}}_D \sqrt{\left(\hat{\dot{x}}_D \right)^2 + \left(\hat{\dot{y}}_D \right)^2} \\
&\quad - k_R \left(\hat{y}_D - \hat{y}_J \right) - k_{NL} \left(\hat{y}_D - \hat{y}_J \right) \left[\left(\hat{x}_D - \hat{x}_J \right)^2 + \left(\hat{y}_D - \hat{y}_J \right)^2 \right] \\
m_J \hat{\ddot{x}}_J &= \hat{F}_X + k_R \left(\hat{x}_D - \hat{x}_J \right) + k_{NL} \left(\hat{x}_D - \hat{x}_J \right) \left[\left(\hat{x}_D - \hat{x}_J \right)^2 + \left(\hat{y}_D - \hat{y}_J \right)^2 \right] \\
m_J \hat{\ddot{y}}_J &= \hat{F}_Y - m_J g + k_R \left(\hat{y}_D - \hat{y}_J \right) + k_{NL} \left(\hat{y}_D - \hat{y}_J \right) \left[\left(\hat{x}_D - \hat{x}_J \right)^2 + \left(\hat{y}_D - \hat{y}_J \right)^2 \right]
\end{aligned} \tag{12}$$

For the non-dimensional parameters, let:

$\tau = \frac{\omega}{2\pi} t$, $x_D = \frac{\hat{x}_D}{g_0}$, $y_D = \frac{\hat{y}_D}{g_0}$, $x_J = \frac{\hat{x}_J}{g_0}$, $y_J = \frac{\hat{y}_J}{g_0}$, $\omega_R^2 = \frac{k_R}{m_D}$, $\omega_{NL}^2 = \frac{k_{NL} g_0^2}{m_D}$, $\varsigma_R = \frac{c_R}{2 m_D \omega_R}$, $\varsigma_{NL} = \frac{c_{NL} g_0}{2 m_D \omega_{NL}}$, $U = \frac{u}{g_0}$, $W = \frac{g}{g_0 \omega_n^2}$, $\lambda = \frac{m_D}{m_J}$, $\eta_R = \frac{\omega_R}{\omega_n}$, $\eta_{NL} = \frac{\omega_{NL}}{\omega_n}$, $\Omega = \frac{\omega}{\omega_n}$, $\lambda = \frac{m_D}{m_J}$, $\Delta_x = x_D - x_J$, $\Delta_y = y_D - y_J$, $\Gamma_D = \left(\dot{x}_D\right)^2 + \left(\dot{y}_D\right)^2$, $P = \frac{\hat{P} g_0}{i_b}$, $D = \frac{\hat{D} \omega_n g_0}{i_b}$.

The non-dimensional system is then written as:

$$\begin{aligned}
\ddot{x}_D &= \left(2\pi\right)^2 U cos\left(2\pi\tau\right) - \left(2\pi\right) \varsigma_R \frac{\eta_R}{\Omega} \dot{x}_D - \varsigma_{ln} \dot{x}_D \sqrt{\Gamma_D \left(\dot{x}_D, \dot{y}_D \right)} \\
&\quad - \left(2\pi\right)^2 \frac{\eta_R^2}{\Omega^2} \Delta_x - \left(2\pi\right)^2 \frac{\eta_{NL}^2}{\Omega^2} \Delta_x \left[\Delta_x^2 + \Delta_y^2 \right] \\
\ddot{y}_D &= \left(2\pi\right)^2 \left(U sin\left(2\pi\tau\right) - \frac{W}{\Omega^2} \right) - \left(2\pi\right) \varsigma_R \frac{\eta_R}{\Omega} \dot{y}_D - \varsigma_{NL} \dot{y}_D \sqrt{\Gamma_D \left(\dot{x}_D, \dot{y}_D \right)} \\
&\quad - \left(2\pi\right)^2 \frac{\eta_R^2}{\Omega^2} \Delta_y - \left(2\pi\right)^2 \frac{\eta_{NL}^2}{\Omega^2} \Delta_y \left[\Delta_x^2 + \Delta_y^2 \right] \\
\ddot{x}_J &= F_X + \left(2\pi\right)^2 \lambda \frac{\eta_R^2}{\Omega^2} \Delta_x + \left(2\pi\right)^2 \lambda \frac{\eta_{NL}^2}{\Omega^2} \Delta_x \left[\Delta_x^2 + \Delta_y^2 \right] \\
\ddot{y}_J &= F_Y - \left(2\pi\right)^2 \frac{W}{\Omega^2} + \left(2\pi\right)^2 \lambda \frac{\eta_R^2}{\Omega^2} \Delta_y + \left(2\pi\right)^2 \lambda \frac{\eta_{NL}^2}{\Omega^2} \Delta_y \left[\Delta_x^2 + \Delta_y^2 \right]
\end{aligned} \tag{13}$$

where the non-dimensional magnetic forces are shown as following:

$$\begin{aligned}
F_X &= F_{X^+} - F_{X^-} + \alpha x_J \left(F_{Y^+} + F_{Y^+} \right) \\
F_Y &= F_{Y^+} - F_{Y^-} + \alpha y_J \left(F_{X^+} + F_{X^+} \right)
\end{aligned}$$

$$
\begin{aligned}
F_{X^+} &= \frac{1}{4\left(P-1\right)}\left(\frac{2\pi}{\Omega}\right)^2 \frac{\left(1-\left(Px_J + D\left(\frac{\Omega}{2\pi}\right)\dot{x}_J\right)\right)^2}{\left(1-x_J\right)^2} \\
F_{X^-} &= \frac{1}{4\left(P-1\right)}\left(\frac{2\pi}{\Omega}\right)^2 \frac{\left(1+\left(Px_J + D\left(\frac{\Omega}{2\pi}\right)\dot{x}_J\right)\right)^2}{\left(1+x_J\right)^2} \\
F_{Y^+} &= \frac{1}{4\left(P-1\right)}\left(\frac{2\pi}{\Omega}\right)^2 \frac{\left(1-\left(Py_J + D\left(\frac{\Omega}{2\pi}\right)\dot{y}_J\right)\right)^2}{\left(1-y_J\right)^2} \\
F_{Y^-} &= \frac{1}{4\left(P-1\right)}\left(\frac{2\pi}{\Omega}\right)^2 \frac{\left(1+\left(Py_J + D\left(\frac{\Omega}{2\pi}\right)\dot{y}_J\right)\right)^2}{\left(1+y_J\right)^2}
\end{aligned} \tag{14}
$$

3 HQM-Based Arc-Length Continuation and Stability Analysis

The Harmonic Quadrature Method (HQM) is a time-domain discretization technique that approximates the periodic solution of a nonlinear dynamical system by evaluating it at a set of equally spaced time nodes over one period, avoiding the costly Galerkin-type integrals inherent in the classical Harmonic Balance Method while retaining high-order accuracy. In the present work, HQM is combined for the first time with pseudo-arc-length continuation and Floquet stability analysis to enable the systematic tracking of both stable and unstable periodic solution branches and the direct detection of saddle-node bifurcation points across the full parameter range of interest.

The periodic solution is discretized over the normalized time interval $\tau \in [0,1]$ using n_τ equally spaced collocation points defined as:

$$
\tau_i = \frac{i}{n_\tau} \tag{15}
$$

The first and second derivative matrices $\left[D_\tau^1\right]$ and $\left[D_\tau^2\right]$ are then constructed from spectral differentiation of the discrete periodic solution vector, following the procedure detailed in [20]. Applying the discretization transforms the governing differential equations into a nonlinear algebraic system evaluated at the collocation points, written explicitly as:

$$
\begin{aligned}
\left[D_\tau^2\right]\{x_D\} &= (2\pi)^2 U\left\{cos\left(2\pi\tau\right)\right\} - (2\pi)\varsigma_R\frac{\eta_R}{\Omega}\left[D_\tau^1\right]\{x_D\} \\
&\quad - (2\pi)^2\frac{\eta_R^2}{\Omega^2}\{\Delta_x\} - (2\pi)^2\frac{\eta_{NL}^2}{\Omega^2}\{\Delta_x\}\left\{\Delta_x^2+\Delta_y^2\right\} \\
&\quad - \varsigma_{NL}\left[D_\tau^1\right]\{x_D\}\left\{\sqrt{\left[D_\tau^1\right]^2\Gamma_D\left(x_D,y_D\right)}\right\} \\
\left[D_\tau^2\right]\{y_D\} &= (2\pi)^2\left(Usin\left(2\pi\tau\right) - \frac{W}{\Omega^2}\{\mathbb{1}\}\right) - (2\pi)\varsigma_R\frac{\eta_R}{\Omega}\left[D_\tau^1\right]\{y_D\} \\
&\quad - (2\pi)^2\frac{\eta_R^2}{\Omega^2}\{\Delta_y\} - (2\pi)^2\frac{\eta_{NL}^2}{\Omega^2}\{\Delta_y\}\left\{\Delta_x^2+\Delta_y^2\right\} \\
&\quad - \varsigma_{NL}\left[D_\tau^1\right]\{y_D\}\left\{\sqrt{\left[D_\tau^1\right]^2\Gamma_D\left(x_D,y_D\right)}\right\} \\
\left[D_\tau^2\right]\{x_J\} &= \{F_X\} + (2\pi)^2\lambda\frac{\eta_R^2}{\Omega^2}\{\Delta_x\} + (2\pi)^2\lambda\frac{\eta_{NL}^2}{\Omega^2}\{\Delta_x\}\left\{\Delta_x^2+\Delta_y^2\right\}
\end{aligned}
$$

$$\left[D_\tau^2\right]\{\ddot{y}_J\} = \{F_Y\} - (2\pi)^2 \frac{W}{\Omega^2}\{\mathbb{1}\} + (2\pi)^2 \lambda \frac{\eta_{NL}^2}{\Omega^2}\{\Delta_y\}\left\{\Delta_x^2 + \Delta_y^2\right\} + (2\pi)^2 \lambda \frac{\eta_R^2}{\Omega^2}\{\Delta_y\} \tag{16}$$

Applying the same collocation discretization to the electromagnetic force expressions of Eqs. (26)–(29), with displacement and velocity terms replaced by their discrete counterparts and the derivative operator $[D_\tau^1]$, yields:

$$\begin{aligned}
F_{X^+} &= \frac{1}{4(P-1)}\left(\frac{2\pi}{\Omega}\right)^2\left(1 - \left[P\{\mathbb{1}\} + D\left(\frac{\Omega}{2\pi}\right)\left[D_\tau^1\right]\right]\{x_J\}\right)^2\left\{(\{\mathbb{1}\} - \{x_J\})^2\right\}^{-1} \\
F_{X^-} &= \frac{1}{4(P-1)}\left(\frac{2\pi}{\Omega}\right)^2\left(1 + \left[P\{\mathbb{1}\} + D\left(\frac{\Omega}{2\pi}\right)\left[D_\tau^1\right]\right]\{x_J\}\right)^2\left\{(\{\mathbb{1}\} + \{x_J\})^2\right\}^{-1} \\
F_{Y^+} &= \frac{1}{4(P-1)}\left(\frac{2\pi}{\Omega}\right)^2\left(1 - \left[P\{\mathbb{1}\} + D\left(\frac{\Omega}{2\pi}\right)\left[D_\tau^1\right]\right]\{y_J\}\right)^2\left\{(\{\mathbb{1}\} - \{y_J\})^2\right\}^{-1} \\
F_{Y^-} &= \frac{1}{4(P-1)}\left(\frac{2\pi}{\Omega}\right)^2\left(1 + \left[P\{\mathbb{1}\} + D\left(\frac{\Omega}{2\pi}\right)\left[D_\tau^1\right]\right]\{y_J\}\right)^2\left\{(\{\mathbb{1}\} + \{y_J\})^2\right\}^{-1}
\end{aligned} \tag{17}$$

The governing equation of motion for the full rotor–bearing model takes the compact operator form:

$$\left(\mathbb{M}\otimes\left[D_\tau^2\right] + \mathbb{C}\otimes\left[D_\tau^1\right] + \mathbb{K}\otimes I\right)\{x\} = \left\{F^{NL}\right\} + \left\{F^R\right\} \tag{18}$$

where the mass, damping, and stiffness operators $\mathbb{M}$, $\mathbb{C}$, and $\mathbb{K}$, the state vector x, and the nonlinear and excitation force vectors F^{NL} and F^R are defined as:

$$\mathbb{M} = \begin{bmatrix} [I] & & & \\ & [I] & & \\ & & [I] & \\ & & & [I] \end{bmatrix},\ \mathbb{C} = \begin{bmatrix} \varsigma_R\frac{\eta_R}{\Omega} & & & \\ & \varsigma_R\frac{\eta_R}{\Omega} & & \\ & & & \\ & & & \end{bmatrix}$$

$$\mathbb{K} = \begin{bmatrix} \frac{\eta_R^2}{\Omega^2}[I] & & -\frac{\eta_R^2}{\Omega^2}[I] & \\ & \frac{\eta_R^2}{\Omega^2}[I] & & -\frac{\eta_R^2}{\Omega^2}[I] \\ -\lambda\frac{\eta_R^2}{\Omega^2}[I] & & \lambda\frac{\eta_R^2}{\Omega^2}[I] & \\ & -\lambda\frac{\eta_R^2}{\Omega^2}[I] & & \lambda\frac{\eta_R^2}{\Omega^2}[I] \end{bmatrix} \tag{19}$$

$$\{x\} = \begin{Bmatrix} x_D(\tau_0) \\ \vdots \\ x_D(\tau_n) \\ - - - \\ y_D(\tau_0) \\ \vdots \\ y_D(\tau_n) \\ - - - \\ x_J(\tau_0) \\ \vdots \\ x_J(\tau_n) \\ - - - \\ y_J(\tau_0) \\ \vdots \\ y_J(\tau_n) \end{Bmatrix}, \left\{F^{NL}\right\} = \begin{Bmatrix} F^{NL}_{x_D}(\tau_0) \\ \vdots \\ F^{NL}_{x_D}(\tau_n) \\ - - - \\ F^{NL}_{y_D}(\tau_0) \\ \vdots \\ F^{NL}_{y_D}(\tau_n) \\ - - - \\ F^{NL}_{x_J}(\tau_0) \\ \vdots \\ F^{NL}_{x_J}(\tau_n) \\ - - - \\ F^{NL}_{y_J}(\tau_0) \\ \vdots \\ F^{NL}_{y_J}(\tau_n) \end{Bmatrix}, \left\{F^{R}\right\} = \begin{Bmatrix} F^{R}_{x_D}(\tau_0) \\ \vdots \\ F^{R}_{x_D}(\tau_n) \\ - - - \\ F^{R}_{y_D}(\tau_0) \\ \vdots \\ F^{R}_{y_D}(\tau_n) \\ - - - \\ F^{R}_{x_J}(\tau_0) \\ \vdots \\ F^{R}_{x_J}(\tau_n) \\ - - - \\ F^{R}_{y_J}(\tau_0) \\ \vdots \\ F^{R}_{y_J}(\tau_n) \end{Bmatrix} \{\mathbb{1}\} = \begin{Bmatrix} 1 \\ \vdots \\ 1 \end{Bmatrix} \tag{20}$$

The individual nonlinear and excitation force vectors are given by:

$$\begin{aligned}
\left\{F^{NL}_{x_D}\right\} &= -\frac{\eta^2_{NL}}{\Omega^2}\{\Delta_x\}\left[\left\{\Delta^2_x\right\} + \left\{\Delta^2_y\right\}\right] - \varsigma_{NL}\left[D^1_\tau\right]\{x_D\}\sqrt{\left[D^1_\tau\right]^2\{\Gamma_D\left(x_D, y_D\right)\}} \\
\left\{F^{NL}_{y_D}\right\} &= -\frac{\eta^2_{NL}}{\Omega^2}\{\Delta_y\}\left[\left\{\Delta^2_x\right\} + \left\{\Delta^2_y\right\}\right] - \varsigma_{NL}\left[D^1_\tau\right]\{y_D\}\sqrt{\left[D^1_\tau\right]^2\{\Gamma_D\left(x_D, y_D\right)\}} \\
\left\{F^{NL}_{x_J}\right\} &= \{F_{X^+}\} - \{F_{X^-}\} + \alpha\{x_J\}\{\{F_{Y^+}\} + \{F_{Y^-}\}\} + \lambda\frac{\eta^2_{NL}}{\Omega^2}\{\Delta_x\}\left[\left\{\Delta^2_x\right\} + \left\{\Delta^2_y\right\}\right] \\
\left\{F^{NL}_{y_J}\right\} &= \{F_{Y^+}\} - \{F_{Y^-}\} + \alpha\{y_J\}\{\{F_{X^+}\} + \{F_{X^-}\}\} + \lambda\frac{\eta^2_{NL}}{\Omega^2}\{\Delta_y\}\left[\left\{\Delta^2_x\right\} + \left\{\Delta^2_y\right\}\right] \\
\left\{F^{R}_{x_D}\right\} &= U\{cos\left(2\pi\tau\right)\} \\
\left\{F^{R}_{y_D}\right\} &= U\{sin\left(2\pi\tau\right)\} - \left\{\frac{W}{\Omega^2}\right\} \\
\left\{F^{R}_{x_J}\right\} &= \{0\} \\
\left\{F^{R}_{y_J}\right\} &= -\left\{\frac{W}{\Omega^2}\right\}
\end{aligned} \tag{21}$$

The final solution is assessed by computing the residual vector $\{R\}$ and verifying that it satisfies the convergence criterion $\left\|R\right\| < \varepsilon = 10^{-8}$:

$$\{R\} = \left(\mathbb{M} \otimes \left[D^2_\tau\right] + \mathbb{C} \otimes \left[D^1_\tau\right] + \mathbb{K} \otimes I\right)\{x\} - \left(\left\{F^{NL}\right\} + \left\{F^{R}\right\}\right) \tag{22}$$

Upon convergence, the time response is evaluated by computing the Fourier coefficient matrix T given by:

$$[[T]] = \begin{bmatrix} 1 & cos(2\pi\tau_0) & sin(2\pi\tau_0) & \cdots & cos(2\pi H\tau_0) & sin(2\pi H\tau_0) \\ \vdots & \vdots & \vdots & \vdots & \vdots & \vdots \\ 1 & cos(2H\tau_{n_\tau}) & sin(2\pi H\tau_{n_\tau}) & \cdots & cos(2\pi H\tau_{n_\tau}) & sin(2\pi H\tau_{n_\tau}) \end{bmatrix} \tag{23}$$

The response is then represented in terms of the Fourier coefficients X as follows:

$$X = [[T]]^{-1} \{x\} \tag{24}$$

where the matrix $[[T]]$ is given by:

$$[[T]] = \begin{bmatrix} [T] & [Z]_{n_\tau} & [Z]_{n_\tau} & [Z]_{n_\tau} \\ [Z]_{n_\tau} & [T] & [Z]_{n_\tau} & [Z]_{n_\tau} \\ [Z]_{n_\tau} & [Z]_{n_\tau} & [T] & [Z]_{n_\tau} \\ [Z]_{n_\tau} & [Z]_{n_\tau} & [Z]_{n_\tau} & [T] \end{bmatrix} \tag{25}$$

The proposed HQM-based arc-length continuation algorithm combines the Harmonic Quadrature Method (HQM) with a predictor--corrector continuation scheme to efficiently compute the nonlinear periodic responses of the rotor system. After applying the HQM discretization, the governing equations are transformed into a nonlinear algebraic system in which the unknowns are the harmonic coefficients X, while the excitation frequency (or rotational speed) is selected as the continuation parameter. The resulting nonlinear system is written as:

$$R(X, s) = 0 \tag{26}$$

where X denotes the vector of harmonic coefficients and s represents the continuation parameter.

For convenience, the solution vector is defined as:

$$U = \begin{Bmatrix} X \\ s \end{Bmatrix} \tag{27}$$

Let $\mathbf{U}_c^i$ denote the converged solution at step i, and let $\mathbf{U}_c^{i+1}$ and $\mathbf{U}_p^{i+1}$ denote the converged and predicted solutions at step $i+1$, respectively, defined as:

$$U_c^i = \begin{Bmatrix} X_c^i \\ s_c^i \end{Bmatrix}, \qquad U_p^{i+1} = \begin{Bmatrix} X_p^{i+1} \\ s_p^{i+1} \end{Bmatrix}, \qquad U_c^{i+1} = \begin{Bmatrix} X_c^{i+1} \\ s_c^{i+1} \end{Bmatrix} \tag{28}$$

Starting from the converged solution U_c^i, the predictor step is performed as:

$$U_p^{i+1} = U_c^i + \Delta_m \, T_i \tag{29}$$

where T_i is the unit tangent vector and Δ_m is the arc-length increment.

The corrector stage is obtained by solving:

$$R(U_c^{i+1}) = 0 \tag{30}$$

subject to the arc-length constraint:

$$(X_c^{i+1} - X_c^i)^T (X_c^{i+1} - X_c^i) + \psi (s_c^{i+1} - s_c^i)^2 = (\Delta_m)^2 \tag{31}$$

The constraint function is written as:

$$g(U_c^{i+1}) = (X_c^{i+1} - X_c^i)^T (X_c^{i+1} - X_c^i) + \psi (s_c^{i+1} - s_c^i)^2 - (\Delta_m)^2 \tag{32}$$

The augmented system solved during correction is given by:

$$\begin{bmatrix} R(U_c^{i+1}) \\ g(U_c^{i+1}) \end{bmatrix} = 0 \tag{33}$$

To assess the stability of each computed periodic solution, a Floquet stability analysis is performed after convergence. The nonlinear system is expressed in state-space form as:

$$\dot{X} = f(X, \tau) \tag{34}$$

Introducing a perturbation $\delta X(\tau)$ gives:

$$\delta\dot{X} = J(\tau)\delta X \tag{35}$$

with:

$$J(\tau) = \left.\frac{\partial f}{\partial X}\right|$$

The state transition matrix satisfies:

$$\dot{\Phi}(\tau) = J(\tau)\Phi(\tau), \qquad \Phi(0) = I \tag{36}$$

The monodromy matrix is defined as:

$$M = \Phi(T) \tag{37}$$

Floquet multipliers are obtained from:

$$\det(M - \mu I) = 0 \tag{38}$$

The system is considered stable when all Floquet multipliers satisfy $|\mu_i| < 1$, and unstable when at least one multiplier satisfies $|\mu_i| > 1$.

Consequently, the combination of HQM, arc-length continuation, and Floquet analysis enables the computation of both stable and unstable periodic branches and provides a complete characterization of the nonlinear dynamic behavior of the rotor system.

4 Numerical Results

The numerical simulations are carried out using the system parameters listed in Table 1. These parameters remain fixed throughout the study unless explicitly stated otherwise. Parametric variations are performed for the proportional gain P, derivative gain D, nonlinear stiffness coefficient η_{NL}, and aerodynamic damping coefficients ζ_{NL} and ζ_R to investigate their influence on the system's nonlinear dynamic behavior. The HQM discretization has

Table 1: Baseline System Parameters

Parameters	P	D	α	ς_R	ς_{NL}	η_R	η_{NL}	λ
Values	4.1	0.5	0.28	0.01	0	0.5	0	5

been previously validated against literature benchmark results in [20, 21] and is adopted here without further validation. Prior to the parametric study, the sensitivity of the computed solutions to the harmonic order H and arc-length step size $\Delta\nu$ is assessed for the looped response (Section 4.3 and Section 4.4), where the topological complexity is significantly greater, convergence is assessed with respect to both harmonic order H and arc-length step size $\Delta\nu$ at $\eta_{NL} = 0.6$ and $P = 4.1$.

Table 2: Harmonic convergence study for the HQM discretization at P = 4.1 and $\eta_{NL} = 0.6$

Harmonics H	3	5	7	9	11
Error %	4.337	1.241	0.525	0.503	0.498

The results, summarized in Table 2 and 3, confirm that the solution converges from 7 harmonics onward and is insensitive to step sizes below $\Delta\nu = 0.01$, with relative errors below 0.52% and 0.3% respectively. Accordingly, 7 harmonics and $\Delta\nu = 0.01$ are adopted for all simulations.

Table 3: Arc length convergence study for the HQM discretization at P = 4.1 and $\eta_{NL} = 0.6$

arc-length step size $\Delta\nu$	0.05	0.01	0.005	0.001
Error %	0.514	0.305	0.301	0.299

4.1 Effect of the Proportional Gain *P* on the Dynamic Response

The proportional gain P is a cornerstone parameter in active magnetic bearing control, as it directly governs the magnitude of the magnetic restoring force and, through the inherent nonlinearity of the electromagnetic force expressions, the degree of nonlinear coupling experienced by the rotor. To unravel its influence on the system's nonlinear dynamics, P is varied from 2 to 4 while all other parameters are held at their baseline values. This variation reveals a rich and progressive evolution of the frequency response, marked by the successive emergence of S-shaped folded branches and regions of multi-stable behavior.

A global view of this evolution is provided by the three-dimensional frequency response surface shown in Fig. 3, which maps the journal displacement amplitude $|y_J|$ as a function of both the nondimensional excitation frequency Ω and the proportional gain P. The surface distinctly captures the primary resonance at the first natural frequency $\frac{\omega_R}{\lambda}$, along with clear superharmonic peaks at $\frac{\omega_R}{2\lambda}$, $\frac{\omega_R}{3\lambda}$ and $\frac{\omega_R}{4\lambda}$. As P increases from 2 to 4, the amplitude at the primary resonance rises significantly, from 0.2328 to 0.3839, confirming that higher proportional gain amplifies the system response by deepening the influence of the magnetic force nonlinearity.

A more detailed examination of the response as a function of P is provided by the heat map in Fig. 4, which reveals the existence of four distinct dynamical regimes. For P ranging from 2 to approximately 2.68, the system exhibits stable, linear-like behavior with a unique solution for each excitation frequency. As P crosses the threshold of approximately 2.69, the first S-shaped nonlinear branch emerges, persisting until $P = 2.75$. Between $P = 2.76$ and $P = 3.0$, the response develops two S-shaped branches, indicating stronger multi-stability. Finally, for P between 3.1 and 4.1, the system enters a highly nonlinear regime characterized by three S-shaped branches and extensive multi-stability. This progression from linear to 1S-shaped, then 2S-shaped, and finally 3S-shaped behavior underscores the critical role of the proportional gain as a bifurcation parameter, through which increasing electromagnetic nonlinearity progressively folds the frequency response curve into successive multi-valued branches.

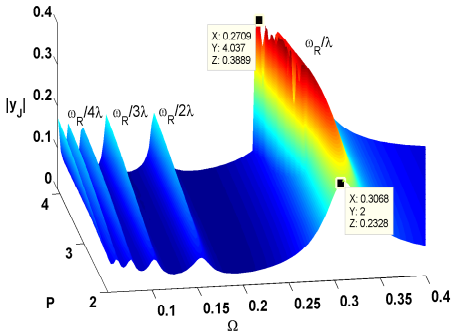

Fig. 3: Three dimensional frequency response surface as a function of Ω.

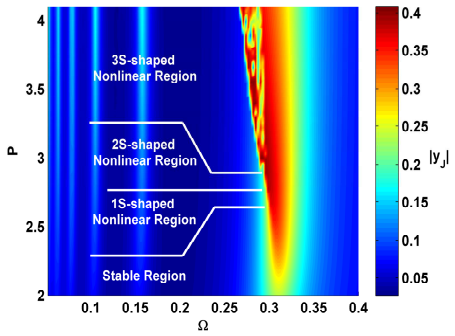

Fig. 4: Heat map of the response amplitude showing four distinct dynamical regimes with respect to P.

To further elucidate the nature of each regime, a representative value of P is selected from each region. In the linear regime, taking $P = 2.4$, the frequency response curve in Fig. 5 displays a smooth, single-peaked profile with no folds or jumps, confirming that the system responds in a quasi-linear manner. The corresponding bifurcation diagram in Fig. 6 verifies the periodic nature of the response: at the primary resonance $\frac{\omega_R}{\lambda}$, the phase portrait exhibits a single closed orbit and the Poincaré map shows a single fixed point. At the superharmonic resonances $\frac{\omega_R}{2\lambda}$, $\frac{\omega_R}{3\lambda}$ and $\frac{\omega_R}{4\lambda}$, the phase portraits reveal 2, 3, and 4 closed curves respectively, with matching multiple points in the Poincaré sections. These observations confirm that the HQM solutions accurately capture the harmonic content of the response, and that the system's periodicity is preserved across all excitation frequencies.

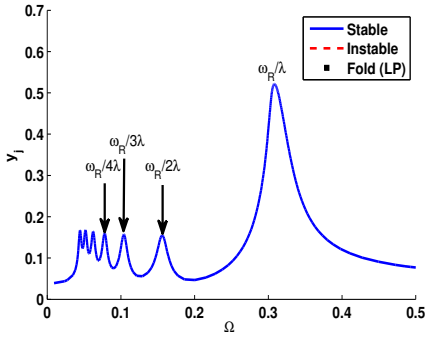

Fig. 5: Frequency response curve for P=2.4 (linear regime)

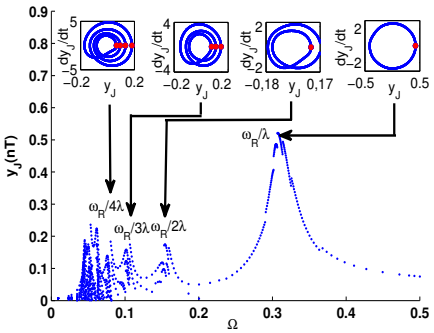

Fig. 6: Bifurcation diagrams for P=2.4: phase portraits and Poincaré maps at primary and superharmonic resonances

At $P = 2.72$, the system transitions into the 1S-shaped nonlinear regime. The frequency response curve in Fig. 7 now exhibits a distinct S-shaped fold, marking the onset of multi-stability near the primary resonance. Floquet stability analysis, shown in Fig. 8, identifies two fold points, $LP1$ and $LP2$, located at $\Omega = 0.2986$ and $\Omega = 0.2989$, respectively. Between these two turning points, the system possesses three coexisting solutions, two stable branches and one unstable branch. The $det(J)$ curve crosses zero at each LP, confirming the saddle-node nature of each bifurcation. The periodicity at the selected frequency $\Omega = 0.2988$ is confirmed

as 1-periodic motion, with a single closed orbit in the phase portrait and a single fixed point in the Poincaré map. This confirms that the nonlinearity introduced by the increased gain P does not alter the fundamental periodicity of the response, and that the observed multi-stability arises purely from the nonlinear force-displacement relationship of the magnetic bearing.

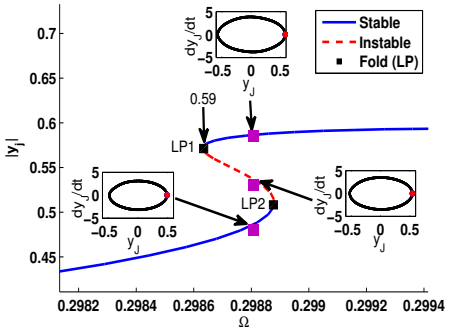

Fig. 7: Frequency response curve for P=2.72 (1S-shaped nonlinear regime)

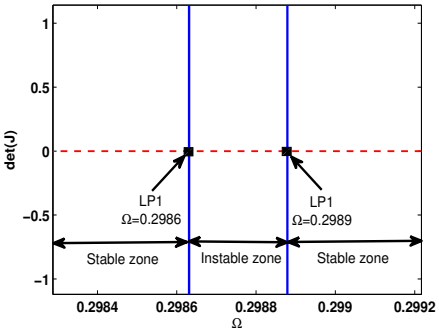

Fig. 8: Fold point detection for P=2.72

For $P = 2.9$, representative of the 2S-shaped regime, the frequency response curve in Fig. 9 shows two distinct S-shaped folded branches, indicating a more complex multi-stable structure. Floquet stability analysis, presented in Fig. 10, detects four fold points, $LP1$ through $LP4$, spanning the frequency interval from $\Omega = 0.2931$ to $\Omega = 0.2969$. The presence of two folded branches indicates that the magnetic force nonlinearity has intensified with the higher gain, leading to additional coexisting stable and unstable branches over a broader frequency range.

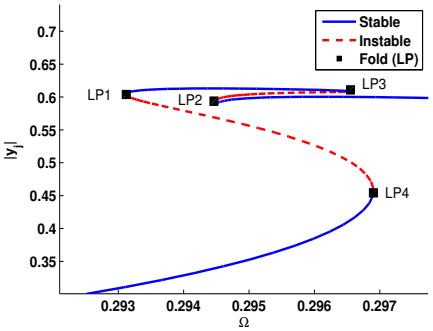

Fig. 9: Frequency response curve for P=2.9 (2S-shaped nonlinear regime)

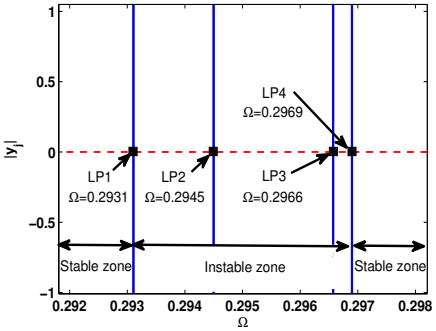

Fig. 10: Fold point detection for P=2.9

At the highest gain investigated, $P = 3.5$, the system enters the 3S-shaped regime, characterized by three S-shaped folded branches in the frequency response curve shown in Fig. 11. Floquet stability analysis, depicted in Fig. 12, identifies eight fold points, $LP1$ through $LP8$, spanning the frequency range from $\Omega = 0.2732$ to $\Omega = 0.2920$. The substantial widening of the unstable frequency band and the increased number of turning points reflect the dominance of the magnetic force nonlinearity at high proportional gain. The system possesses

multiple coexisting stable solutions over a broad frequency band, significantly increasing the risk of amplitude jumps and hysteresis in practice.

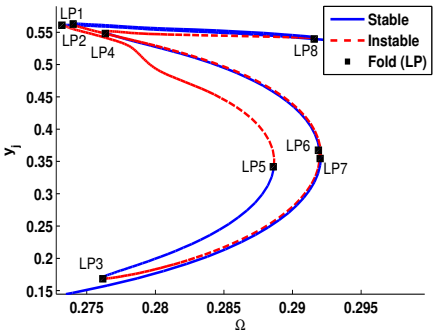

Fig. 11: Frequency response curve for P=3.5 (3S-shaped nonlinear regime)

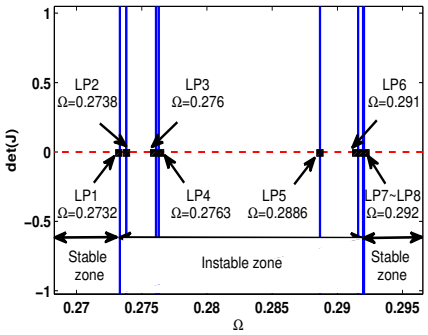

Fig. 12: Fold point detection for P=3.5

4.2 Effect of the Derivative Gain D on the Dynamic Response

While the proportional gain P was shown to promote the emergence of multi-stability through magnetic force nonlinearity, the derivative gain D plays a fundamentally opposing role by introducing electromagnetic damping into the control loop. This damping is proportional to the journal velocity, acting to resist motion rather than displacement and thereby attenuating the oscillatory behavior that P amplifies. To investigate this stabilizing effect, D is varied from 0.5 to 2.5 while P is held at its baseline value of 4.1, which places the system firmly in the 3S-shaped nonlinear regime at the outset.

The three-dimensional frequency response surface in Fig. 13 illustrates the evolution of the system's response as a function of both the excitation frequency Ω and the derivative gain D. In striking contrast to the effect of P, increasing D progressively attenuates the vibration amplitude across the entire frequency range. The peak amplitude at the primary resonance decreases significantly from 0.3534 at $D = 0.5$ to 0.1598 at $D = 2.5$, confirming that higher derivative gain introduces electromagnetic damping that effectively suppresses the system's nonlinear response.

The heat map in Fig. 14 reveals three distinct dynamical regimes as D increases. For low derivative gain in the range $0.5 \leq D \leq 1.16$, the system exhibits strong multi-stability characterized by three S-shaped folded branches, as the electromagnetic damping is insufficient to overcome the folding driven by the magnetic force nonlinearity. As D increases to the interval $1.16 \leq D \leq 1.23$, the nonlinearity is partially suppressed and the system transitions to a single S-shaped folded branch, indicating that the derivative gain has begun to regularize the frequency response. For $D \geq 1.23$, the response becomes quasi-linear, with no loops or folds, indicating that the derivative gain has effectively stabilized the system by eliminating the multi-stable branches. This 3S, 1S and linear progression is the exact inverse of the cascade driven by P, revealing a symmetric and complementary relationship between the two control gains, P creates bifurcation complexity through magnetic stiffness nonlinearity, and D systematically destroys it through electromagnetic damping.

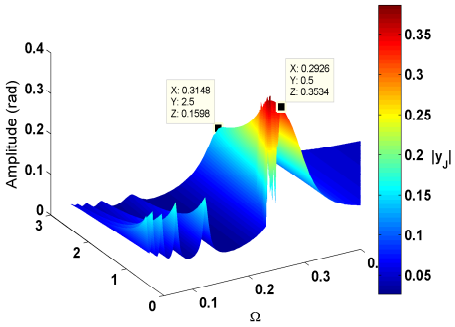

Fig. 13: Three-dimensional frequency response surface as a function of Ω and D

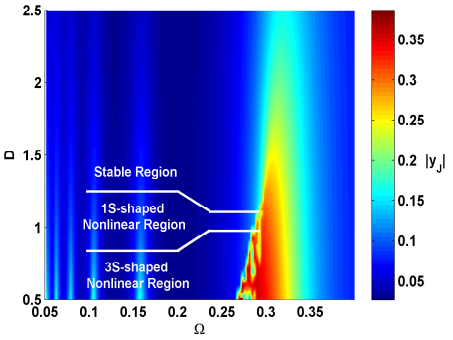

Fig. 14: Heat map of the response amplitude showing three distinct dynamical regimes with respect to D

To further illustrate this inverse cascade, representative values of D are selected from each regime. At $D = 0.8$, characteristic of the 3S regime, the frequency response curve in Fig. 15 displays three distinct S-shaped folded branches, indicating extensive multi-stability. Floquet stability analysis, shown in Fig. 16, identifies eight fold points,$LP1$ through $LP8$, spanning the frequency range from $\Omega = 0.2798$ to $\Omega = 0.2925$. The presence of multiple turning points over a wide frequency band confirms that low derivative gain allows the magnetic force nonlinearity to dominate the system's response, producing a bifurcation topology equivalent to that observed at high P.

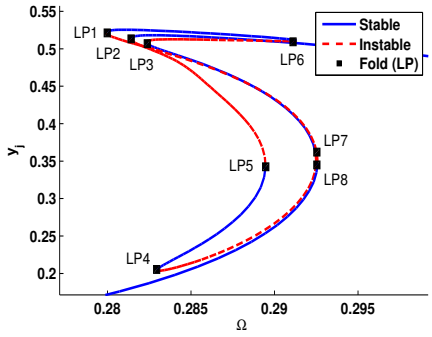

Fig. 15: Frequency response curve for D=0.8 (3S-shaped nonlinear regime)

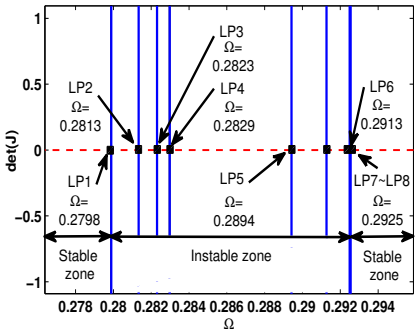

Fig. 16: Fold point detection for D=0.8

At $D = 1.22$, representative of the 1S regime, the frequency response curve in Fig. 17 exhibits a single S-shaped branch, indicating that the increased damping has partially suppressed the nonlinearity. Floquet analysis, presented in Fig. 18, detects only two fold points, $LP1$ and $LP2$,located at Ω=0.2963 and Ω=0.2965, with an unstable frequency range that is now extremely narrow spanning less than 0.0005 in nondimensional frequency. This dramatic narrowing of the unstable zone, from a width of 0.0127 at D = 0.8 to less than 0.0005 at D = 1.22, quantitatively reflects the progressive stabilizing influence of the derivative gain.

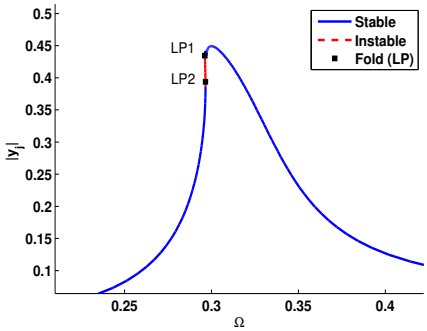

Fig. 17: Frequency response curve for D=1.22 (1S-shaped nonlinear regime)

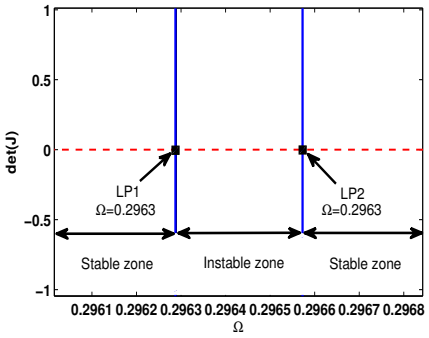

Fig. 18: Fold point detection for D=1.22

Finally, at $D = 2.0$, representative of the linear regime, the frequency response curve in Fig. 19 exhibits a single smooth peak with no folds. The system now possesses a unique stable solution at every excitation frequency, and the derivative gain has effectively eliminated all multi-stability induced by the magnetic force nonlinearity. The response amplitude is significantly reduced compared to lower D values, confirming the combined amplitude-suppressing and stability-restoring role of the derivative gain.

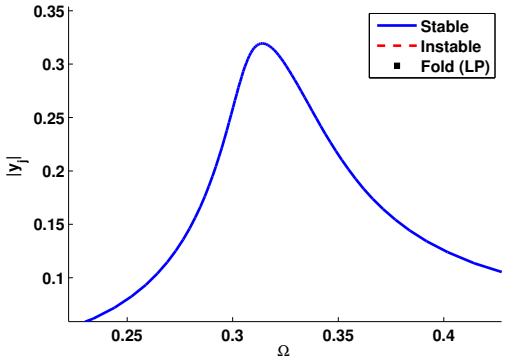

Fig. 19: Frequency response curve for D=2.0 (linear regime)

4.3 Effect of the Nonlinear Stiffness Coefficient η_{NL} on the Dynamic Response

Having established the roles of P and D in shaping the S-shaped bifurcation topology through the magnetic force nonlinearity, attention is now directed to the effect of the nonlinear shaft stiffness coefficient η_{nl}, which introduces a hardening mechanical nonlinearity of opposite sign to the softening magnetic nonlinearity. The system is fixed at $P = 4.1$ and $D = 0.5$, placing it in the 3S-shaped nonlinear regime, and η_{NL} is varied from 0 to 0.6 to investigate the interaction between these two competing nonlinear mechanisms.

The three-dimensional frequency response surface in Fig. 20 and the corresponding heat map in Fig. 21 provide a global picture of this interaction. For low values of η_{NL}, the system remains in the 3S-shaped nonlinear region previously characterized, with the response topology governed predominantly by the magnetic force nonlinearity. As η_{NL} increases beyond the critical threshold $\eta_{NL} = 0.5$, a qualitatively new phenomenon emerges, the 3S-shaped backbone develops a looped sub-structure, as identified in Fig. 21 by the 3S-shaped Looped Nonlinear Region. This transition marks the onset of a new bifurcation regime that cannot be produced by either nonlinearity acting alone, it is the direct consequence of the competition between the softening magnetic nonlinearity and the hardening cubic stiffness nonlinearity as previously demonstrated in [21], where closed-loop branches were obtained under the combined effect of nonlinear structural forces and nonlinear Hertzian contact forces.

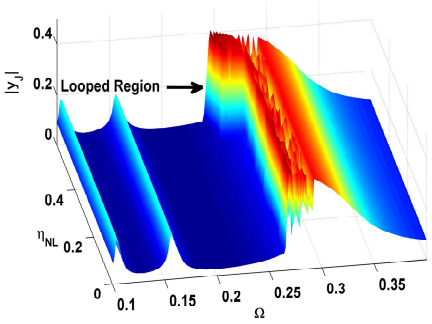

Fig. 20: Three-dimensional frequency response surface as a function of Ω and η_{NL}

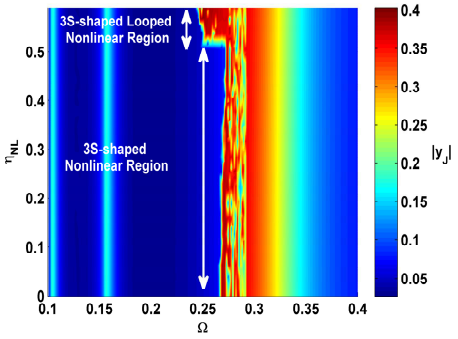

Fig. 21: Heat map of the response amplitude showing the 3S-shaped regime and the looped region with respect to η_{NL}

The most striking manifestation of this competition is observed at$\eta_{NL} = 0.55$. The frequency response curve in Fig. 22 reveals a complex connected closed-loop branch superimposed on the 3S-shaped backbone. The inset provides a magnified view of the loop interior, clearly showing alternating stable and unstable arcs separated by a large number of fold points. Floquet stability analysis in Fig. 23 confirms the presence of more than 36 fold points, labeled $LP_i, i > 36$ and spanning the wide frequency interval from $\Omega = 0.2466$ to $\Omega = 0.2922$. This extensive unstable zone, covering a nondimensional frequency range of approximately 0.0456, represents a dramatic broadening of the multi-stable region compared to the clean 3S structure observed at $\eta_{NL} = 0$. Within this interval, the system possesses a large number of coexisting stable and unstable periodic solutions, making the response history-dependent and practically unpredictable without a complete bifurcation map. Each fold point is individually verified by a zero crossing of the $det(J)$ curve, confirming the Floquet-verified saddle-node nature of every turning point. Importantly, the loop remains connected to the main frequency response branch at both ends, distinguishing it from an isolated resonance curve and confirming that the phenomenon is a topological transformation of the existing 3S branch rather than the emergence of a disconnected solution family.

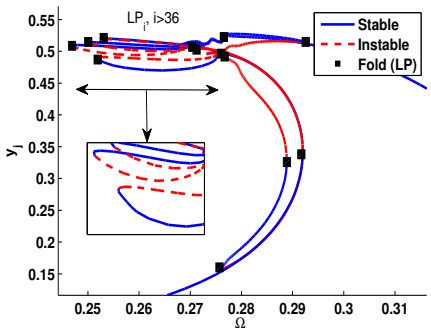

Fig. 22: Frequency response curve for η_{NL}=0.55 showing 3S-shaped backbone with loop proliferation

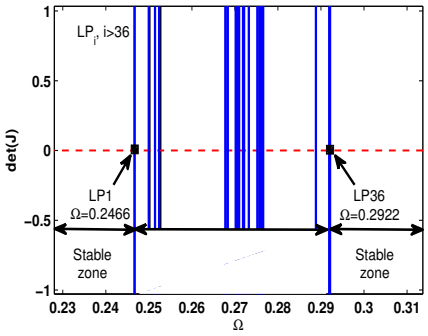

Fig. 23: Fold point detection for η_{NL}=0.55

To establish the physical origin of this loop proliferation and to confirm that it is not a numerical artifact, the magnetic and cubic forces are extracted separately and compared for two representative values of η_{NL}. At $\eta_{NL} = 0.001$, shown in Fig. 24 and Fig. 26, the cubic force exhibits a maximum amplitude of approximately 2.5×10^{-5} , negligible compared to the magnetic force maximum of approximately 125. At this value, the cubic force presents small loops and the system's response is governed predominantly by the magnetic bearing forces, resulting in the clean 3S-shaped behavior with no loop formation. At $\eta_{NL} = 0.55$, shown in Fig. 25 and Fig. 27, the magnetic force retains a similar shape with a slightly increased maximum of approximately 140, confirming that the magnetic force is relatively insensitive to η_{NL} and acts as the background restoring mechanism. In striking contrast, the cubic force now reaches a maximum of approximately 12, an increase of nearly five orders of magnitude and exhibits a proliferation of loops whose topology directly mirrors the loops observed in the displacement frequency response. The ratio of cubic to magnetic force increases from approximately 0.002% at $\eta_{NL} = 0.001$ to approximately 8.6% at $\eta_{NL} = 0.55$, identifying a critical force ratio threshold beyond which the hardening cubic nonlinearity is sufficiently strong to compete with and distort the softening magnetic nonlinearity, generating the observed loop structure. These force comparison results provide definitive physical evidence that the loop proliferation is a genuine nonlinear dynamic phenomenon driven by the interaction of two competing force mechanisms, rather than a numerical artifact of the continuation algorithm.

In summary, the nonlinear stiffness coefficient η_{NL} introduces a hardening mechanical nonlinearity that competes directly with the softening magnetic force nonlinearity. For small η_{NL}, the magnetic force dominates and the system exhibits the clean 3S-shaped topology. As η_{NL} increases toward a critical threshold, identified here at approximately $\eta_{NL} = 0.5$, the cubic force reaches sufficient magnitude to interact with the magnetic nonlinearity, generating a connected closed-loop branch containing more than 36 fold points and a dramatically broadened unstable frequency zone.

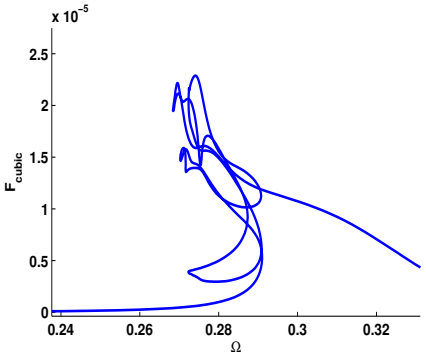

Fig. 24: Cubic force for η_{NL}=0.001

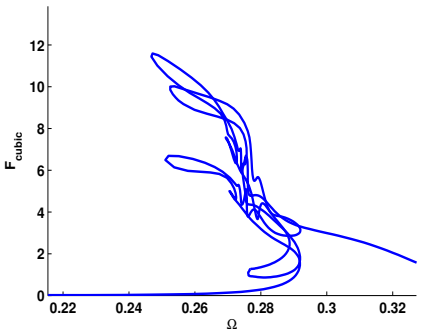

Fig. 25: Cubic force for η_{NL}=0.55

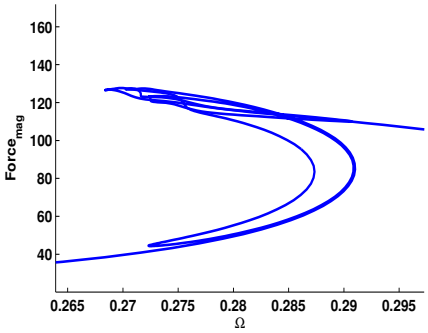

Fig. 26: Magnetic force for η_{NL}=0.001

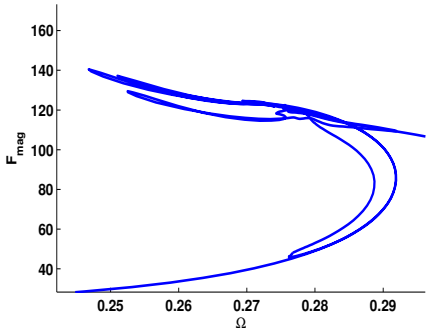

Fig. 27: Magnetic force for η_{NL}=0.55

4.4 Effect of Aerodynamic Damping, ς_{NL} and ς_R, on the Dynamic Response

Damping plays a crucial role in shaping the nonlinear frequency response of the rotor system. The present model incorporates two physically distinct aerodynamic damping mechanisms, the linear damping coefficientζ_R, which represents viscous air resistance dominant at low rotational speeds and small vibration amplitudes, and the nonlinear damping coefficientζ_{NL}, which accounts for turbulent aerodynamic drag dominant at high rotational speeds and large vibration amplitudes. To elucidate their respective roles, the two mechanisms are studied independently and then directly compared.

The nonlinear damping coefficient ζ_{NL} is first varied from 0.1 to 1.0 while the linear damping is set to zero ($\zeta_R = 0$). The heat map in Fig. 28 and the three-dimensional frequency response surface in Fig. 29 reveal that increasing ζ_{NL} immediately suppresses any form of multi-stability, effectively eliminating S-shaped loops and restoring single-valued behavior across the entire frequency range. This rapid suppression is consistent with the amplitude-squared dependence of the turbulent drag force, at the primary resonance where journal amplitudes are large, the nonlinear damping force grows quadratically with amplitude and dominates the energy dissipation, preventing the large-amplitude folding that produces the S-shaped branches. However, the superharmonic resonances, where vibration amplitudes are

significantly smaller, remain largely unaffected by variations in ζ_{NL}, confirming that nonlinear turbulent damping primarily targets high-amplitude dynamics while having negligible influence on low-amplitude harmonic peaks.

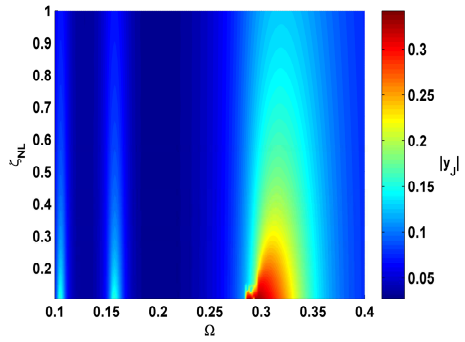

Fig. 28: Heat map of the response amplitude with respect to ζ_{NL} ($\zeta_R = 0$)

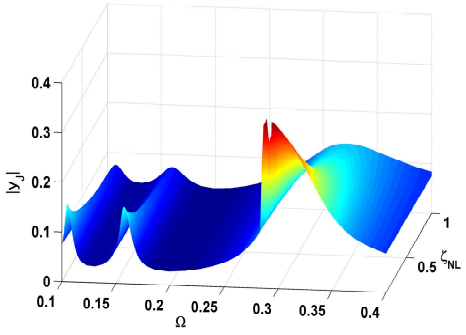

Fig. 29: Three-dimensional frequency response surface as a function of Ω and ζ_{NL} ($\zeta_R = 0$)

The linear damping coefficient ζ_R is then varied from 0.01 to 0.1 while the nonlinear damping is set to zero ($\zeta_{NL} = 0$). The heat map in Fig. 30 and the corresponding three-dimensional surface in Fig. 31 reveal a qualitatively different behavior, increasing ζ_R primarily reduces the amplitude of the superharmonic resonances, while its attenuating effect on the primary resonance is comparatively moderate. This contrasting behavior reflects the linear proportionality of the viscous drag force to velocity, at small amplitudes, where velocity magnitudes are modest, the linear drag force remains active and provides effective damping of the low-amplitude superharmonic peaks, at the large amplitudes of the primary resonance, the linear force is less competitive compared to the nonlinear terms, resulting in less efficient suppression.

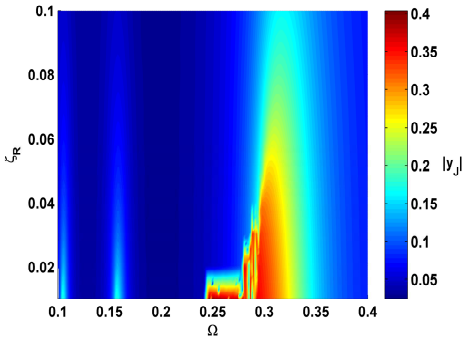

Fig. 30: Heat map of the response amplitude with respect to ζ_R ($\zeta_{NL} = 0$)

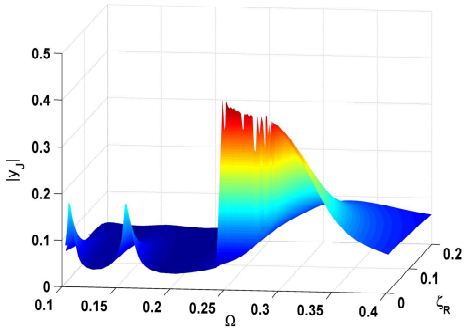

Fig. 31: Three-dimensional frequency response surface as a function of Ω and ζ_R ($\zeta_{NL} = 0$)

To directly and quantitatively compare the two damping mechanisms, the frequency response curves for two representative cases are superimposed in Fig. 32, pure nonlinear damping with $\zeta_{NL} = 0.4$ and $\zeta_R = 0$, and pure linear damping with $\zeta_R = 0.04$ and $\zeta_{NL} = 0$. At the primary resonance, nonlinear damping reduces the journal amplitude to 0.1959,

whereas linear damping reduces it only to 0.3071, a difference of 36%, clearly demonstrating the superior attenuation efficiency of the turbulent drag at large amplitudes. Conversely, at the first superharmonic resonance, nonlinear damping attenuates the amplitude to 0.099, while linear damping achieves a slightly stronger attenuation to 0.091, confirming the relative advantage of linear damping at small-amplitude harmonic peaks.

The physical origin of this amplitude-dependent regime transition is directly revealed by the damping force comparison in Fig. 33, which plots the linear and nonlinear damping forces as functions of excitation frequency. At the primary resonance frequency, the nonlinear damping force is significantly larger than its linear counterpart, explaining its superior attenuation of the primary peak. At the superharmonic resonance frequency, the linear damping force exceeds the nonlinear damping force, consistent with the observation that linear damping is more effective at small-amplitude higher harmonics. A crossover point between the two force curves is clearly visible near $\Omega \approx 0.27$, marking the transition between the amplitude regime where linear damping dominates and the amplitude regime where nonlinear damping dominates. This crossover provides a direct physical explanation for the different attenuation characteristics observed in Figs. 15 and 16, and justifies the inclusion of both damping mechanisms in the present model, a model retaining only linear damping would significantly overestimate the primary resonance amplitude, while a model retaining only nonlinear damping would fail to accurately predict the superharmonic peak attenuation.

In summary, the two aerodynamic damping mechanisms exhibit complementary and amplitude-dependent roles in governing the nonlinear frequency response. Nonlinear turbulent damping is highly effective at suppressing the primary resonance and eliminating multi-stability, but has negligible influence on superharmonic peaks. Linear viscous damping provides moderate attenuation at the primary resonance but is more effective at reducing superharmonic amplitudes.

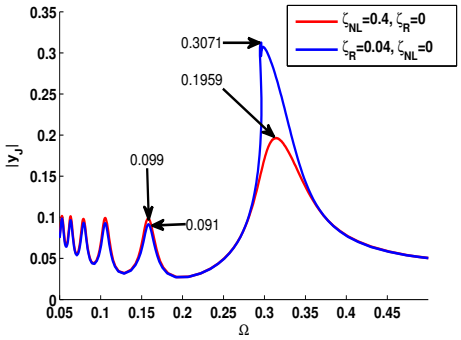

Fig. 32: Superposed FRCs comparing nonlinear and linear damping effects

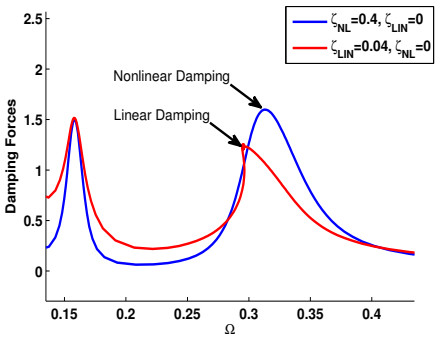

Fig. 33: Comparison of linear and nonlinear damping forces as a function of frequency

5 Discussion

The results presented in this study reveal a rich and layered nonlinear dynamic behavior in the AMB-supported flexible rotor system, driven by the interplay of three distinct nonlinear mechanisms: the softening electromagnetic force nonlinearity, the hardening cubic shaft stiffness nonlinearity, and the amplitude-dependent aerodynamic damping. Each mechanism

contributes a qualitatively distinct signature to the frequency response, and their interactions produce bifurcation phenomena that cannot be predicted or characterized by linearized models or weakly nonlinear perturbation methods.

The progressive S-shaped bifurcation cascade driven by the proportional gain P is perhaps the most practically significant finding from a controller design perspective. The existence of four clearly bounded dynamical regimes, linear, 1S-shaped, 2S-shaped, and 3S-shaped, mapped as a function of both P and the excitation frequency Ω, provides a quantitative design chart that an AMB engineer can directly exploit. Specifically, the identification of $P = 2.68$ as the threshold beyond which the first fold bifurcation emerges means that proportional gains below this value guarantee single-valued, globally stable operation regardless of initial conditions or speed history. Above this threshold, the system enters a regime where amplitude jumps and hysteresis become possible, and the response amplitude at any given frequency depends on the path taken to reach it. This path-dependence has direct implications for rotor run-up and run-down procedures in industrial AMB systems: a rotor sweeping upward through a frequency band containing a fold bifurcation may jump to a high-amplitude state that it would not reach under downward frequency sweeping, a phenomenon well known in nonlinear oscillator theory but rarely characterized quantitatively for AMB rotor systems in the manner presented here.

The inverse cascade produced by increasing the derivative gain D is equally significant and complements the P result in a physically transparent way. The symmetric relationship between P and D one creating bifurcation complexity, the other systematically destroying it, provides a clear and actionable control strategy, for any AMB rotor operating in the 3S nonlinear regime due to high P, a derivative gain of $D \geq 1.23$ is sufficient to fully eliminate multi-stability and restore safe single-valued operation. This result establishes a quantitative stability boundary in the (P, D) control parameter space, which is a practically useful output that existing perturbation-based AMB rotor studies cannot provide due to their amplitude restrictions. It is worth noting that this stabilizing role of D is distinct from its classical role as a noise amplifier in PD control, while large D is generally avoided in practice due to sensor noise sensitivity, the present results suggest that a moderate increase in D within the range $1.16 \leq D \leq 1.23$ can achieve the transition from 3S to linear behavior without requiring excessively large derivative action. This narrow transition band, spanning only $\Delta_D = 0.07$, highlights the sensitivity of the bifurcation topology to the derivative gain in this parameter range and suggests that fine-tuned D adjustment could serve as a practical stability control mechanism in AMB systems operating near the nonlinear regime boundary.

The most theoretically significant result of this study is the connected closed-loop branch containing more than 36 fold points, identified at $\eta_{NL} = 0.55$ with the system fixed in the 3S regime. This phenomenon deserves careful physical interpretation. The loop arises because the softening magnetic nonlinearity which tends to bend the resonance curve toward lower frequencies with increasing amplitude, producing the S-shaped folds is opposed by the hardening cubic stiffness nonlinearity, which tends to bend the curve toward higher frequencies. When the cubic force reaches a sufficient fraction of the magnetic force approximately 8.6% in the present case, the two competing tendencies create a highly folded branch topology in which the frequency response curve folds back on itself many times within a narrow frequency band, producing the large number of alternating stable and unstable segments observed. This mechanism is analogous in principle to the mixed hardening-softening Duffing oscillator, where opposite-sign nonlinear terms are known to produce complex multi-valued responses, but the specific realization in an AMB rotor system with position-dependent electromagnetic forces and cubic shaft stiffness has not been previously reported. The connected nature of the loop, confirmed by the continuation algorithm and consistent with the uniqueness of periodic solutions in the full phase space, distinguishes this result from isolated resonance curves

reported in purely softening oscillator systems, and reflects the specific balance between the two competing nonlinearities that prevents the loop from detaching into a fully isolated branch. From an engineering standpoint, the 36+ fold points imply an extraordinarily large number of coexisting stable periodic solutions within the frequency interval $\Omega \in [0.2466, 0.2922]$, making the rotor response in this range strongly history-dependent and essentially unpredictable without a complete bifurcation map of the kind provided here. In practice, a rotor operating in this parameter regime could settle into any of the many coexisting stable states depending on startup conditions, speed history, or external perturbations, with potentially large amplitude differences between states, a situation that poses serious challenges for safe AMB operation and that motivates the development of active stabilization strategies capable of guiding the rotor to a desired low-amplitude state.

The amplitude-dependent damping regime transition identified in Section 4.4 provides a physically grounded justification for the dual-damping formulation adopted in this work and has implications beyond the specific system studied here. The identification of a crossover frequency near $\Omega \approx 0.27$, below which linear viscous damping dominates and above which nonlinear turbulent damping dominates, means that a model retaining only one damping mechanism will systematically mispredict the response in the frequency range governed by the other. Specifically, a purely linear damping model would overestimate the primary resonance amplitude by approximately 57% compared to the nonlinear damping case ($0.3071 vs 0.1959$), while a purely nonlinear damping model would slightly underestimate the superharmonic peak attenuation. For high-speed AMB rotors operating across a wide speed range, from low-speed startup through multiple superharmonic resonances to the primary resonance, this dual-damping formulation is therefore not merely a theoretical refinement but a practical modeling necessity. The result also has implications for experimental identification of AMB rotor damping: measurements taken only near the primary resonance will characterize the nonlinear turbulent drag but will not capture the linear viscous contribution that governs superharmonic behavior, and vice versa. A complete experimental damping characterization therefore requires measurements across both amplitude regimes.

The three-parameter interaction identified in this study, P driving complexity, D suppressing it, and η_{NL} transforming it, suggests that the nonlinear dynamic behavior of AMB rotors is far more sensitive to the combination of control and mechanical parameters than existing linearized or weakly nonlinear analyses indicate. The complete bifurcation maps provided, the (Ω, P) stability chart, the (Ω, D) stability chart, and the (Ω, η_{NL}) loop formation chart, collectively constitute a practical design reference for AMB engineers seeking to avoid or exploit nonlinear dynamic phenomena in high-speed rotor applications.

6 Conclusion

This study has presented a comprehensive numerical investigation of the nonlinear dynamic behavior of a flexible rotor supported by active magnetic bearings, incorporating cubic shaft stiffness and nonlinear aerodynamic drag, using a Harmonic Quadrature Method combined with pseudo-arc-length continuation and Floquet stability analysis.

The proportional gain P is identified as a key bifurcation parameter that drives a progressive S-shaped cascade through four distinct dynamical regimes as it increases from 2 to 4: a linear regime for P ¡ 2.68, a 1S-shaped nonlinear regime for $2.69 \leq P \leq 2.75$, a 2S-shaped regime for $2.76 \leq P \leq 3.0$, and a 3S-shaped regime for $3.1 \leq P \leq 4.1$. Each transition is accompanied by an increasing number of Floquet-verified saddle-node bifurcation points and a progressive widening of the multi-stable frequency band, driven by the deepening influence of the magnetic force nonlinearity at higher proportional gain. The derivative gain D is shown

to produce the exact inverse cascade, systematically destroying the multi-stability created by P and restoring quasi-linear behavior for D $\geq$ 1.23, establishing a quantitative stability boundary in the control parameter space and revealing a symmetric and complementary bifurcation relationship between the two control gains.

When the nonlinear stiffness coefficient η_{NL} is introduced at fixed P in the 3S regime, the competing hardening mechanical nonlinearity interacts with the softening magnetic nonlinearity to generate a connected closed-loop branch containing more than 36 Floquet-verified saddle-node bifurcation points spanning the frequency interval $\Omega \in [0.2466, 0.2922]$. Force comparison analysis confirms that this phenomenon is physically driven by the growth of the cubic-to-magnetic force ratio from 0.002% to 8.6% at the loop onset threshold, representing the most complex nonlinear dynamic behavior identified in the study and underscoring the critical role of shaft stiffness nonlinearity in AMB rotor systems operating under high proportional gain.

An amplitude-dependent aerodynamic damping regime transition is further identified, in which nonlinear turbulent damping governs the primary resonance while linear viscous damping is more effective at attenuating superharmonic peaks. The crossover in damping force magnitudes near $\Omega \approx 0.27$ defines the frequency threshold separating these two regimes and provides physical justification for the dual-damping formulation adopted in this work, demonstrating that a model retaining only one damping mechanism would systematically mispredict the response across part of the frequency range.

Collectively, these findings provide a comprehensive characterization of the nonlinear bifurcation topology of AMB-supported rotor systems under combined nonlinearities, with direct implications for safe proportional-derivative controller tuning and rotor dynamic prediction. Future work will investigate the incorporation of squeeze film dampers and floating ring bearings as passive stabilization mechanisms to extend the safe operating range of AMB systems to higher proportional gains, and will explore nonlinear control strategies capable of actively suppressing the connected loop formation identified in the present study.

Declarations

- **Funding:** The Article Processing Charge (APC) for the publication of this work was waived. This work did not receive any financial funding.
- **Conflict of interest:** The authors declare that they have no known competing financial interests or personal relationships that could have appeared to influence the work reported in this paper.
- **Ethics approval and consent to participate:** Not applicable.
- **Consent for publication:** Not applicable.
- **Data availability:** The data that support the findings of this study are available from the corresponding author upon reasonable request.
- **Materials availability:** Not applicable.
- **Code availability:** Not applicable.
- **Author contribution:** The authors contributed equally to this work.

References

1. Ahad MA, Iqbal N, Ahmad SM, et al (2021) Detailed modelling and lqg ltr control of a 2-dof radial active magnetic bearing for rigid rotor. Journal of the Brazilian

Society of Mechanical Sciences and Engineering 43(234). https://doi.org/10.1007/s40430-021-02951-4

2. Rosa FC, Lima F, Fumagalli MA (2016) A high-speed shaft supported by magnetic bearings applied to energy systems. Journal of the Brazilian Society of Mechanical Sciences and Engineering 39:29–39. https://doi.org/10.1007/s40430-016-0650-3

3. Eissa MH, Hegazy UH, Amer YA (2007) Dynamic behavior of an amb supported rotor subject to harmonic excitation. Applied Mathematical Modelling 32:1370–1380. https://doi.org/10.1016/j.apm.2007.04.005

4. Su Y, Gu Y, Keogh PS, et al (2020) Nonlinear dynamic simulation and parametric analysis of a rotor-amb-tdb system experiencing strong base shock excitations. Mechanism and Machine Theory 155:104071. https://doi.org/10.1016/j.mechmachtheory.2020.104071

5. Soni T, Dutt JK, Das AS (2019) Parametric stability analysis of active magnetic bearing supported rotor system with a novel control law subject to periodic base motion. IEEE Transactions on Industrial Electronics 67:1160–1170. https://doi.org/10.1109/tie.2019.2898604

6. Ebrahimi R, Ghayour M, Khanlo HM (2017) Effects of some design parameters on bifurcation behavior of a magnetically supported coaxial rotor in auxiliary bearings. Engineering Computations 34:2379–2395. https://doi.org/10.1108/ec-04-2017-0141

7. Eissa M, Saeed NA, El-Ganini WA (2013) Saturation-based active controller for vibration suppression of a four-degree-of-freedom rotor–amb system. Nonlinear Dynamics 76:743–764. https://doi.org/10.1007/s11071-013-1166-3

8. Han Q, He R (2018) Torsional dynamics and stability of automotive driveline considering cubic nonlinearity. Proceedings of the Institution of Mechanical Engineers Part D Journal of Automobile Engineering 233:2203–2212. https://doi.org/10.1177/0954407018779655

9. Phadatare HP, Pratiher B (2019) Nonlinear modeling, dynamics, and chaos in a large deflection model of a rotor–disk–bearing system under geometric eccentricity and mass unbalance. Acta Mechanica 231:907–928. https://doi.org/10.1007/s00707-019-02559-9

10. Yan S, Dowell EH, Lin B (2014) Effects of nonlinear damping suspension on nonperiodic motions of a flexible rotor in journal bearings. Nonlinear Dynamics 78:1435–1450. https://doi.org/10.1007/s11071-014-1526-7

11. Phadatare HP, Pratiher B (2020) Dynamic stability and bifurcation phenomena of an axially loaded flexible shaft-disk system supported by flexible bearing. Proceedings of the Institution of Mechanical Engineers Part C Journal of Mechanical

Engineering Science 234:2951–2967. https://doi.org/10.1177/0954406220911957

12. Thaljaoui F, Trabelssi M, Chiboub MH (2023) A study of magnetic parameters in the performance and stability of a blade-installed energy harvester. In: 2023 IEEE International Conference on Artificial Intelligence and Green Energy (ICAIGE). IEEE, Sousse, Tunisia, pp 1–6

13. Tang D, Dowell EH (1997) Nonlinear rotor aeroelastic analysis with stall and advanced wake dynamics. Journal of Aircraft 34:679–687. https://doi.org/10.2514/2.2229

14. Hu GC, Xiang JW, Zhang XG (2003) Dynamic stability analysis for helicopter rotor/fuselage coupled nonlinear systems. Chinese Journal of Aeronautics 16:22–28. https://doi.org/10.1016/s1000-9361(11)60166-0

15. Ferguson K, Thomson D (2014) Flight dynamics investigation of compound helicopter configurations. Journal of Aircraft 52:156–167. https://doi.org/10.2514/1.c032657

16. Gu Q, Yang J, Zhang W, et al (2021) An accelerating sweep frequency excitation method for the rotordynamic coefficients identification of annular gas seals based on computational fluid dynamics. Journal of Engineering for Gas Turbines and Power 143(9). https://doi.org/10.1115/1.4051101

17. Motallebi A, Irani S, Sazesh S (2015) Analysis on jump and bifurcation phenomena in the forced vibration of nonlinear cantilever beam using hbm. Journal of the Brazilian Society of Mechanical Sciences and Engineering 38:515–524. https://doi.org/10.1007/s40430-015-0352-2

18. Kim S, Palazzolo A (2018) Shooting/continuation based bifurcation analysis of large order nonlinear rotordynamic systems. MATEC Web of Conferences 211:18003. https://doi.org/10.1051/matecconf/201821118003

19. Holl HJ (2000) An efficient semi-analytic time integration method with application to non-linear rotordynamic systems. Computational Mechanics 26:362–375. https://doi.org/10.1007/s004660000184

20. Thaljaoui F, Hili M, Trabelssi M (2025) Nonlinear multi-harmonic response of a misaligned rotor under base vibration motion using the harmonic quadrature method. Journal of the Brazilian Society of Mechanical Sciences and Engineering 47(7). https://doi.org/10.1007/s40430-025-05653-3

21. Thaljaoui F, Trabelssi M, Hili M (2023) Implementation of a new approach based on harmonic quadrature method on the study of a misaligned rotor supported in ball bearings squeeze film system. In: Advances in Acoustics and Vibration IV. Springer, pp 328–341